

Atomic-Level Regulated 2D ReSe₂: A Universal Platform Boostin Photocatalysis

Jingrun Ran, Ling Chen, Deyu Wang, Amin Talebian-Kiakalaieh, Yan Jiao, Mahmoud Adel Hamza, Yang Qu, Liqiang Jing, Kenneth Davey, and Shi-Zhang Qiao*

Solar hydrogen (H₂) generation via photocatalytic water splitting is practically promising, environmentally benign, and sustainably carbon neutral. It is important therefore to understand how to controllably engineer photocatalysts at the atomic level. In this work, atomic-level engineering of defected ReSe₂ nanosheets (NSs) is reported to significantly boost photocatalytic H₂ evolution on various semiconductor photocatalysts including TiO₂, CdS, ZnIn₂S₄, and C₃N₄. Advanced characterizations, such as atomic-resolution aberration-corrected scanning transmission electron microscopy (AC-STEM), synchrotron-based X-ray absorption near edge structure (XANES), in situ X-ray photoelectron spectroscopy (XPS), transient-state surface photovoltage (SPV) spectroscopy, and transient-state photoluminescence (PL) spectroscopy, together with theoretical computations confirm that the strongly coupled ReSe₂/TiO₂ interface and substantial atomic-level active sites of defected ReSe₂ NSs result in the significantly raised activity of ReSe₂/TiO₂. This work not only for the first time realizes the atomic-level engineering of ReSe₂ NSs as a versatile platform to significantly raise the activities on different photocatalysts, but, more importantly, underscores the immense importance of atomic-level synthesis and exploration on 2D materials for energy conversion and storage.

to carbon-free/clean hydrogen (H₂) fuel via environmentally benign and low cost photocatalysis is of significant interest.^[1–29] However, reported efficiencies for photocatalytic H₂ evolution are practically poor.

Rational design and synthesis of highly efficient and robust photocatalysts requires an accurate understanding of atomic-level composition/structure-performance correlation,^[6,7,21,23,25–32] and thermodynamics/kinetics of light-induced charge carriers in photocatalysts.^[3,4,6,9–13,16–24,26,28–32] Hence, advanced characterizations including, aberration-corrected scanning transmission electron microscopy (AC-STEM), synchrotron-based X-ray absorption near edge structure (XANES), in situ X-ray photoelectron spectroscopy (XPS), transient-state photoluminescence spectroscopy (TSPL), and transient-state surface photovoltage spectroscopy (TSSPV), are usually combined with density functional theory (DFT) computations, to reveal atomic-scale structure/composition-

activity relationship and charge dissociation/transfer dynamics.^[6,21,23,25,26,28–32]

2D transitional metal chalcogenides (TMCs) are a wide variety of materials applied in many fields, such as catalysis,^[33–50] energy storage,^[39,51] and (opto)electronics.^[52,53] As a typical TMC, 2D ReSe₂, exhibits intriguing advantages: 1) alterable electronic bandgap width to balance light absorption range and redox abilities of photo-induced electrons/holes; 2) ultrathin thickness to facilitate bulk-to-surface charge migration; 3) large surface area to enable strong electronic coupling with other materials; 4) numerous edge active sites.^[33–48] Nevertheless, 2D ReSe₂ is rarely adopted for photocatalysis. Additionally, atomic-level and controlled engineering of 2D ReSe₂ to optimize physicochemical properties for high efficiency photocatalysis is not reported.


In this work for the first time, we report atomic-level and controlled engineering of 2D ReSe₂ via sonication-assisted liquid exfoliation to synthesize ReSe₂ nanosheets (NSs) with abundant in situ generated edge defects. Theoretical computation confirms existence of abundant active sites along edge-defected ReSe₂ for hydrogen evolution reaction (HER). We demonstrate atomic-level engineered ReSe₂ NSs as a universal platform to couple with different photocatalysts including metal oxide (TiO₂), metal sulfides (CdS and ZnIn₂S₄), and metal-free nitride (C₃N₄) to achieve significantly-boosted H₂ evolution.

1. Introduction

Continued burning of finite fossil fuels is accelerating environmental contamination and global warming with climate change. Therefore, transformation of renewable solar energy

J. Ran, L. Chen, D. Wang, A. Talebian-Kiakalaieh, Y. Jiao, M. Adel Hamza, K. Davey, S.-Z. Qiao
School of Chemical Engineering and Advanced Materials
The University of Adelaide
Adelaide, South Australia 5005, Australia
E-mail: s.qiao@adelaide.edu.au

Y. Qu, L. Jing
Key Laboratory of Functional Inorganic Material Chemistry
(Ministry of Education)
School of Chemistry and Materials Science
International Joint Research Center for Catalytic Technology
Heilongjiang University
Harbin 150080, China

 The ORCID identification number(s) for the author(s) of this article can be found under <https://doi.org/10.1002/adma.202210164>.

© 2023 The Authors. Advanced Materials published by Wiley-VCH GmbH. This is an open access article under the terms of the Creative Commons Attribution License, which permits use, distribution and reproduction in any medium, provided the original work is properly cited.

DOI: 10.1002/adma.202210164

Via advanced characterizations and theoretical computation, we confirm intense electronic interaction between ReSe₂ NSs and TiO₂ NPs, together with atomic-scale active sites of ReSe₂ NSs result in the high activity. Our work not only demonstrates that the as-synthesized ReSe₂ NSs act as the versatile platform to greatly raise photocatalytic H₂ evolution, but also provides insights into the atomic-level design/synthesis of TMC based materials toward renewable energy conversion/storage.

2. Results and Discussion

2.1. ReSe₂ NS and its combination with various photocatalysts

A facile and sonication-assisted liquid-exfoliation route was developed to synthesize ReSe₂ nanosheets (NSs) with plentiful edge defects. In detail, bulk ReSe₂ was ground in an agate mortar and sonicated in an ice bath for 6 h. This route not only exfoliated bulk ReSe₂ to ReSe₂ NSs, but also selectively generated abundant defects along the edge of ReSe₂ NSs. This is because that strong sonication generates local-area high temperature and pressure via cavitation effect^[54] that helps break the relatively weaker Re-Se chemical bond(s) at the edge of ReSe₂, but not the stronger Re-Se bond(s) in the basal plane of ReSe₂.

To confirm this, atomic-resolution HAADF-STEM images of ReSe₂ NSs with Re vacancy (V_{Re}) and corresponding intensity profiles were obtained (Figure 1a–h). All atomic-resolution HAADF-STEM images of ReSe₂ NSs were obtained using low electron dose to avoid electron beam induced generation/evolution of defects. Notably, Figure S1 (Supporting Information) show the same images as Figure 1a,c,e,g, respectively. As annotated in Figure S1 (Supporting Information), Figure 1a,c show ReSe₂ (010) edge; while Figure 1e,g display ReSe₂ (100) edge. According to intensity profiles (Figure 1b,d,f,h), Figure 1a,c exhibit ReSe₂ (010) edge with one and two V_{Re} , respectively; while Figure 1e-g display ReSe₂ (100) edge with one and two V_{Re} , respectively. In contrast, no V_{Re} is observed in the basal plane for ReSe₂ NSs, as indicated by the HAADF-STEM image (Figure S2a,b, Supporting Information) and corresponding intensity profile (Figure S2c, Supporting Information) of ReSe₂ NSs basal plane. To confirm these ReSe₂ edge defects were generated during exfoliation, atomic-resolution HAADF-STEM images and corresponding intensity profiles for bulk ReSe₂ were determined (Figure S3, Supporting Information). Based on intensity profiles (Figure S3c,f, Supporting Information), no V_{Re} was observed along the (010) and (100) edge of bulk ReSe₂. Additionally, no V_{Re} was found in the atomic-resolution HAADF-STEM image of bulk ReSe₂ basal plane (Figure S4a,b, Supporting Information). The Raman spectra for bulk ReSe₂ and ReSe₂ NSs (Figure 1i) exhibit peaks in the range 100–300 cm⁻¹, resulting from complexity of lattice vibrations in triclinic phase ReSe₂.^[55,56] The peaks at 122/123 cm⁻¹ are attributed to E_g-like in-plane vibration mode, and peaks at 157/159 and 171/173 cm⁻¹ are attributed to A_g-like out-of-plane vibration mode (Figure 1i). Figure 1i also shows that all peaks for ReSe₂ NSs shift to the left, compared with those for bulk ReSe₂. This could arise from generation of defects in ReSe₂ NSs during exfoliation of bulk ReSe₂.^[5] As shown in Table S1 (Supporting

Information), bulk ReSe₂ shows the Se/Re atomic ratios of 1.852 and 1.516, based on inductively coupled plasma atomic emission spectroscopy (ICP-AES) and energy-dispersive X-ray spectroscopy (EDS), respectively. These results indicate the existence of Se vacancies in bulk ReSe₂. This is further corroborated by the atomic-resolution HAADF-STEM image and corresponding intensity profile (Figure S4a–c, Supporting Information), indicating the existence of V_{Se} and absence of V_{Re} in the basal plane of bulk ReSe₂. In contrast, after exfoliation, ReSe₂ NSs exhibit the raised Se/Re atomic ratios of 1.925 and 1.690, based on ICP-AES and EDS, respectively (Table S1, Supporting Information). These results are attributed to the in situ generation of abundant V_{Re} along the edge of ReSe₂ NSs, as evidenced by atomic-resolution HAADF-STEM images (Figure 1a,c,e,g) and corresponding intensity profiles (Figure 1b,d,f,h). Furthermore, the atomic-resolution HAADF-STEM image (Figure S2a,b, Supporting Information) and corresponding intensity profiles (Figure S2c and d) for the basal plane of ReSe₂ NSs suggest the absence of V_{Re} and existence of V_{Se} in the basal plane of ReSe₂ NSs. As shown in Figure S5 (Supporting Information), HER activity of ReSe₂ NSs is significantly raised than that of bulk ReSe₂, indicating existence of much more active sites in ReSe₂ NSs compared with those in bulk ReSe₂. Notably, ReSe₂ NSs has current density of ≈ -0.261 mA cm⁻² at 0 V versus RHE in Figure S5 (Supporting Information), arising from the capacitive current of high-surface-area catalysts.^[57]

To reveal the atomic-level HER active sites of edge defected ReSe₂, density functional theory (DFT) computations were conducted to determine the values for hydrogen adsorption Gibbs energy (ΔG_{H^*}) on 58 sites at basal plane (Figure S6a,b, Supporting Information), (010) edge (Figure S6c,d, Supporting Information), (100) edge (Figure S6e,f, Supporting Information), defected (010) edge (Figure S7a–d, Supporting Information), and defected (100) edge (Figure S7e–h, Supporting Information) of ReSe₂ monolayer. Corresponding ΔG_{H^*} values for these 58 sites are shown in Tables S2–S8 (Supporting Information). Atomic structures showing computed active sites are displayed in Figure S7a,c,e,g (Supporting Information), and corresponding HER diagrams are shown in Figure S7b,d,f,h (Supporting Information), respectively. Besides, we have also calculated the ΔG_{H^*} values on 16 sites at the basal plane of four types of ReSe₂ monolayers with one V_{Se} (Figure S8a–h and Tables S9–S12, Supporting Information). All the computed active sites are highlighted in red color. Based on these findings, it is concluded as follows: 1) no active sites are in the basal plane of non-defected ReSe₂ because of the largely positive values for ΔG_{H^*} (Figure S6a,b and Table S2, Supporting Information), rendering it difficult for proton adsorption; 2) no active sites exist at the edge of ReSe₂ without defect, although the edge sites show significantly lower values for $|\Delta G_{\text{H}^*}|$ (Figure S6c–f and Tables S3 and S4, Supporting Information) compared with those at the basal plane of ReSe₂; 3) there are abundant active sites at the edge of ReSe₂ with one or two V_{Re} (Figure S7 and Tables S5–S8, Supporting Information); 4) these are some active sites at the basal plane of ReSe₂ monolayers with one V_{Se} (Figure S8c–f and Tables S10 and S11, Supporting Information). Among all these active sites, some are highly active as confirmed by near-zero $|\Delta G_{\text{H}^*}|$ values, for example, Se2 at ReSe₂ (010) edge with one V_{Re} ($\Delta G_{\text{H}^*} = 0.05$ eV; Figure S7a,b and Table S5, Supporting

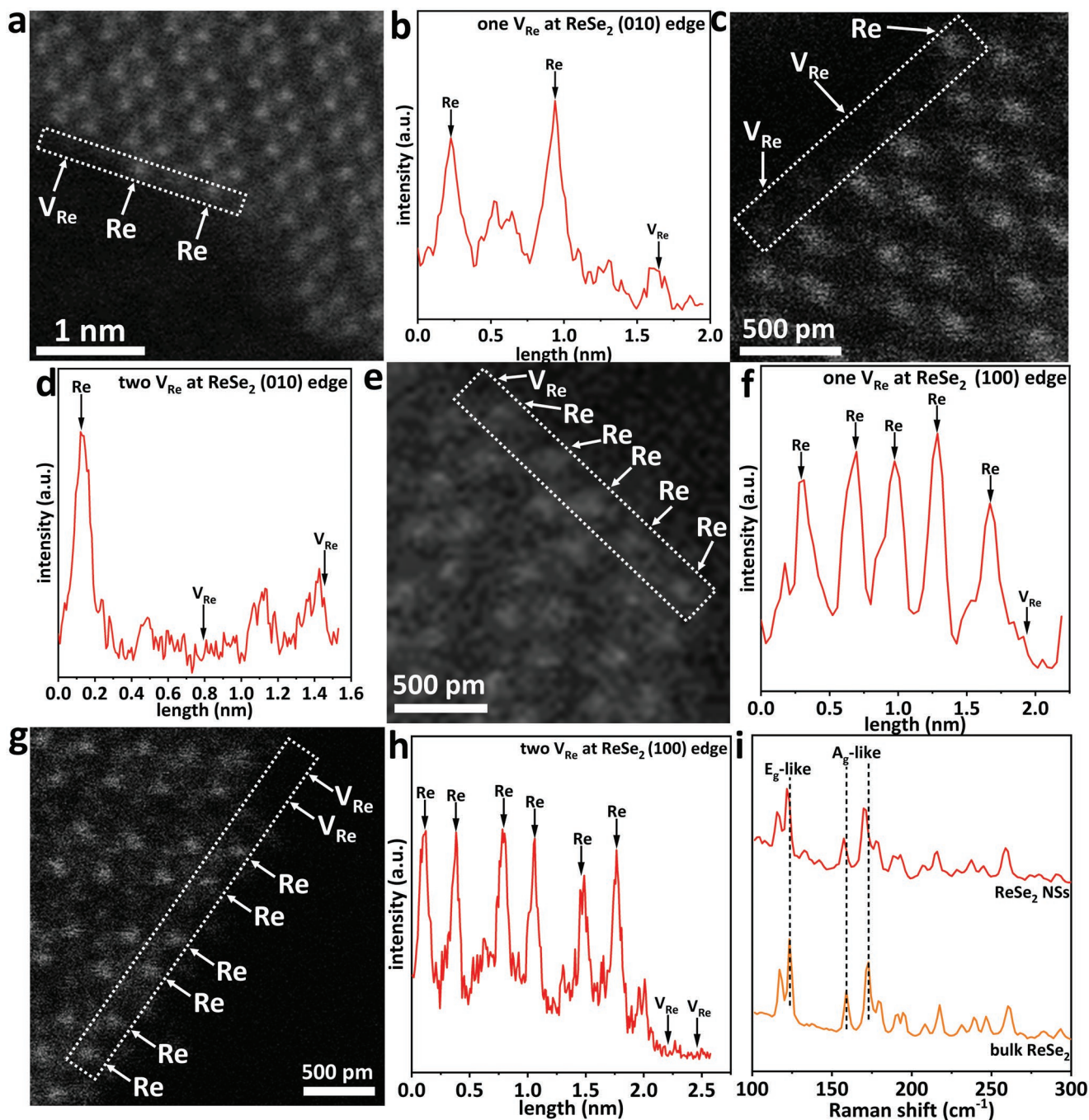


Figure 1. a) Atomic-Resolution low-dose HAADF-STEM image of ReSe₂ (010) edge with one V_{Re} and b) the corresponding intensity profile showing the existence of one V_{Re}. c) Atomic-Resolution low-dose HAADF-STEM image of ReSe₂ (010) edge with two V_{Re} and d) the corresponding intensity profile showing the existence of two V_{Re}. e) Atomic-resolution low-dose HAADF-STEM image of ReSe₂ (100) edge with one V_{Re} and f) the corresponding intensity profile exhibiting the existence of one V_{Re}. g) Atomic-resolution low-dose HAADF-STEM image of ReSe₂ (100) edge with two V_{Re} and h) the corresponding intensity profile displaying the existence of two V_{Re}. i) Raman spectra of bulk ReSe₂ and ReSe₂ NSs. Brightness of (a,c,e,g) was increased to highlight atoms of ReSe₂.

Information) and Se6 at ReSe₂ (100) edge with one V_{Re} ($\Delta G_{H^*} = -0.05$ eV; Figure S7e,f and Table S7, Supporting Information). Theoretical computations disclose existence of 17 Re/Se active sites along the (010) and (100) edge of defected ReSe₂, in agreement with atomic-resolution HAADF-STEM images of defected ReSe₂ (Figure 1a,c,e,g) and HER activity (Figure S5,

Supporting Information). Additionally, three Re/Se active sites are located in the basal plane of two types of ReSe₂ monolayers with one V_{Se} (Figure S8c–f, Supporting Information).

The atomic force microscopy (AFM) image of ReSe₂ NSs (Figure S9a, Supporting Information) exhibits lateral sizes of ≈ 250 – 320 nm. Accordingly, the height profile for ReSe₂

NSs (Figure S9b, Supporting Information) exhibits a thickness of ≈ 11.8 nm. The HAADF-STEM images of ReSe_2 NSs (Figure S10a, Supporting Information) and EDX elemental mapping images of Re (Figure S10b, Supporting Information) and Se (Figure S10c, Supporting Information) for ReSe_2 NSs confirm successful synthesis of ReSe_2 NSs. Transmission electron microscopy (TEM) images of ReSe_2 NSs (Figure S11a, Supporting Information) exhibit lateral size of ≈ 100 – 230 nm. The high-resolution (HR)TEM images of ReSe_2 NSs (Figure S11b, Supporting Information) exhibit two inter-planar distances, of 0.17 and 0.21 nm, with an angle of 51.3° corresponding to the (4-20) and (210) facets for triclinic ReSe_2 , respectively. This is in accordance with the corresponding FFT pattern of ReSe_2 NSs (Figure S11c, Supporting Information). The energy dispersive X-ray spectroscopy (EDX) spectrum for ReSe_2 NSs (Figure S11d, Supporting Information) indicates existence of Re and Se elements, in accordance with the above results. Furthermore, many TEM images of ReSe_2 NSs have been collected to establish the lateral size distribution and thickness distribution of ReSe_2 NSs in Figure S12a,b (Supporting Information), respectively. For ReSe_2 NSs, Figure S12a (Supporting Information) shows an average lateral size of 158.7 nm while Figure S12b (Supporting Information) exhibits an average thickness distribution of 25.6 nm. Furthermore, the XRD pattern of ReSe_2 NSs is in accordance with the standard XRD pattern of triclinic-phase ReSe_2 (JCPDS #52-0828; Figure S13, Supporting Information). Further observation on Figure S13 (Supporting Information) indicates the slight right shift of XRD peaks for ReSe_2 NSs compared to those of standard ReSe_2 , due to the existence of Re/Se vacancies in the crystal structure. This is also in agreement with the HAADF-STEM images of ReSe_2 NSs. The high-resolution XPS spectra of Re 4f and Se 3d for ReSe_2 NSs are shown in Figure S14a,b (Supporting Information), respectively. As shown in Figure S15a (Supporting Information), the diffuse reflectance UV–vis–NIR absorption spectra of powder-form ReSe_2 NSs and bulk ReSe_2 exhibit the absorption edges at 1158 and 1251 nm, corresponding to the band gaps of 1.07 and 0.99 eV, respectively. The blue-shifted band edge and increased bandgap of ReSe_2 NSs compared to bulk ReSe_2 arise from the reduced lateral size and thickness. Notably, the bandgap of ReSe_2 NSs is narrower than the reported value,^[22] due to the existence of abundant vacancies in the crystal structure. The Mott–Schottky (MS) plot for ReSe_2 NSs (Figure S15b, Supporting Information) exhibits a flat band potential of -0.47 V versus Ag/AgCl electrode. Therefore, the Fermi level (E_F) for ReSe_2 NSs is determined to be -0.47 V versus Ag/AgCl electrode, equivalent to 0.16 V versus standard hydrogen electrode (SHE). The XPS valence band (VB) spectrum of ReSe_2 NSs (Figure S15c, Supporting Information) shows that the VB edge potential of ReSe_2 NSs is 0.62 V versus E_F . As a result, the VB edge potential of ReSe_2 NSs is 0.78 V versus SHE. Therefore, the conduction band (CB) edge potential of ReSe_2 NSs is -0.29 V versus SHE. Thus, the CB edge potential of ReSe_2 NSs (Figure S16, Supporting Information) is more negative than H_2 evolution potential (0.0 V vs SHE), suggesting that the photo-induced electrons on the CB of ReSe_2 NSs can reduce protons to gaseous H_2 . The photo-induced holes in the VB of ReSe_2 NSs possess weak oxidation ability (0.78 V vs SHE; Figure S16, Supporting Information), which cannot realize oxygen evolution

reaction (1.23 V vs SHE). Given the numerous edge Re/Se active sites, excellent charge mobility but weak oxidation ability of holes, ReSe_2 NSs should be coupled by other photocatalyst(s) with strongly oxidative holes rather than used alone for photocatalytic H_2 evolution.

Therefore, we have dispersed different photocatalysts including TiO_2 , CdS, ZnIn_2S_4 , and C_3N_4 , respectively, on ReSe_2 NSs. The samples were annotated, respectively, $\text{ReSe}_2/\text{TiO}_2$, ReSe_2/CdS , $\text{ReSe}_2/\text{ZnIn}_2\text{S}_4$, and $\text{ReSe}_2/\text{C}_3\text{N}_4$. The photocatalytic H_2 evolution activity for each is shown in Figure 2a. Importantly, it is seen in Figure 2a that in comparison with bare samples (TiO_2 , CdS, ZnIn_2S_4 or C_3N_4), hybridized samples exhibit significantly boosted H_2 evolution. Especially, $\text{ReSe}_2/\text{TiO}_2$ displays a tremendous raise on photocatalytic H_2 evolution ($2081 \mu\text{mol h}^{-1} \text{g}^{-1}$, $\approx 9048\%$ times greater than that for TiO_2). This is the greatest enhancement factor among the four coupled samples (Figure 2a). Therefore, advanced characterization and theoretical computation were collectively undertaken to determine the origin for high activity on $\text{ReSe}_2/\text{TiO}_2$. Given that photocatalytic H_2 evolution of $\text{ReSe}_2/\text{TiO}_2$ occurred in ≈ 17 vol.% triethanolamine aqueous solution, all theoretical computations were carried out considering the solvation effect in 17 vol.% triethanolamine aqueous solution.

2.2. Structures and Compositions of $\text{ReSe}_2/\text{TiO}_2$ Composites

The 6.0, 50.0, 62.0, and 83.0 mL of ReSe_2 NSs ethanol solutions, were, respectively, combined with 50 mg TiO_2 NPs via self-assembly using physical mixing. Accordingly, samples obtained were annotated, respectively, 6.0RT, 50.0RT, 62.0RT, and 83.0RT. Bare TiO_2 NPs were denoted as 0.0RT. A HAADF-STEM image of 0.0RT (TiO_2 NPs in Figure S17a, Supporting Information) exhibits the sizes of ≈ 19 – 35 nm. Elemental mapping images for Ti (Figure S17b, Supporting Information) and O (Figure S17c, Supporting Information) are in accordance with HAADF-STEM image of TiO_2 NPs. High-resolution HAADF-STEM image of TiO_2 NPs (Figure S17d, Supporting Information) show the lattice spacing of 0.37 nm, attributed to the (100) crystal facet of anatase TiO_2 . As shown in Figure S18 (Supporting Information), the Raman spectrum of 0.0RT (TiO_2 NPs) exhibits several characteristic bands in the range 100– 700 cm^{-1} . These are attributed to Ti–O stretching modes [A_{1g} , $B_{1g(2)}$, $E_{g(3)}$] and Ti–O–Ti deformations [$E_{g(1)}$, $B_{1g(1)}$] of anatase TiO_2 .^[23] The as-synthesized samples were characterized via X-ray diffraction (XRD). XRD patterns for 0.0RT, 6.0RT, 50.0RT, 62.0RT, and 83.0RT are given in Figure S19 (Supporting Information). Compared with the XRD peaks for 0.0RT, the peaks assigned to anatase and rutile phase of TiO_2 for $\text{ReSe}_2/\text{TiO}_2$ composites display the gradually reduced intensities (Figure S19, Supporting Information). This is because of gradually decreased contents of TiO_2 in 6.0RT ($\approx 96.83\%$), 50.0RT ($\approx 78.55\%$), 62.0RT ($\approx 74.71\%$) and 83.0RT ($\approx 68.81\%$), as estimated from the concentration of ReSe_2 NSs ($\approx 273.04 \mu\text{g mL}^{-1}$) determined by ICP-AES.

No peak shifts were evident in the patterns for $\text{ReSe}_2/\text{TiO}_2$ composites (6.0RT, 50.0RT, 62.0RT, and 83.0RT) in comparison with that for 0.0RT (TiO_2). The reason is that, the room-temperature physical coupling of ReSe_2 with TiO_2 did not alter the crystal/phase structure in anatase and rutile TiO_2 . Additionally,

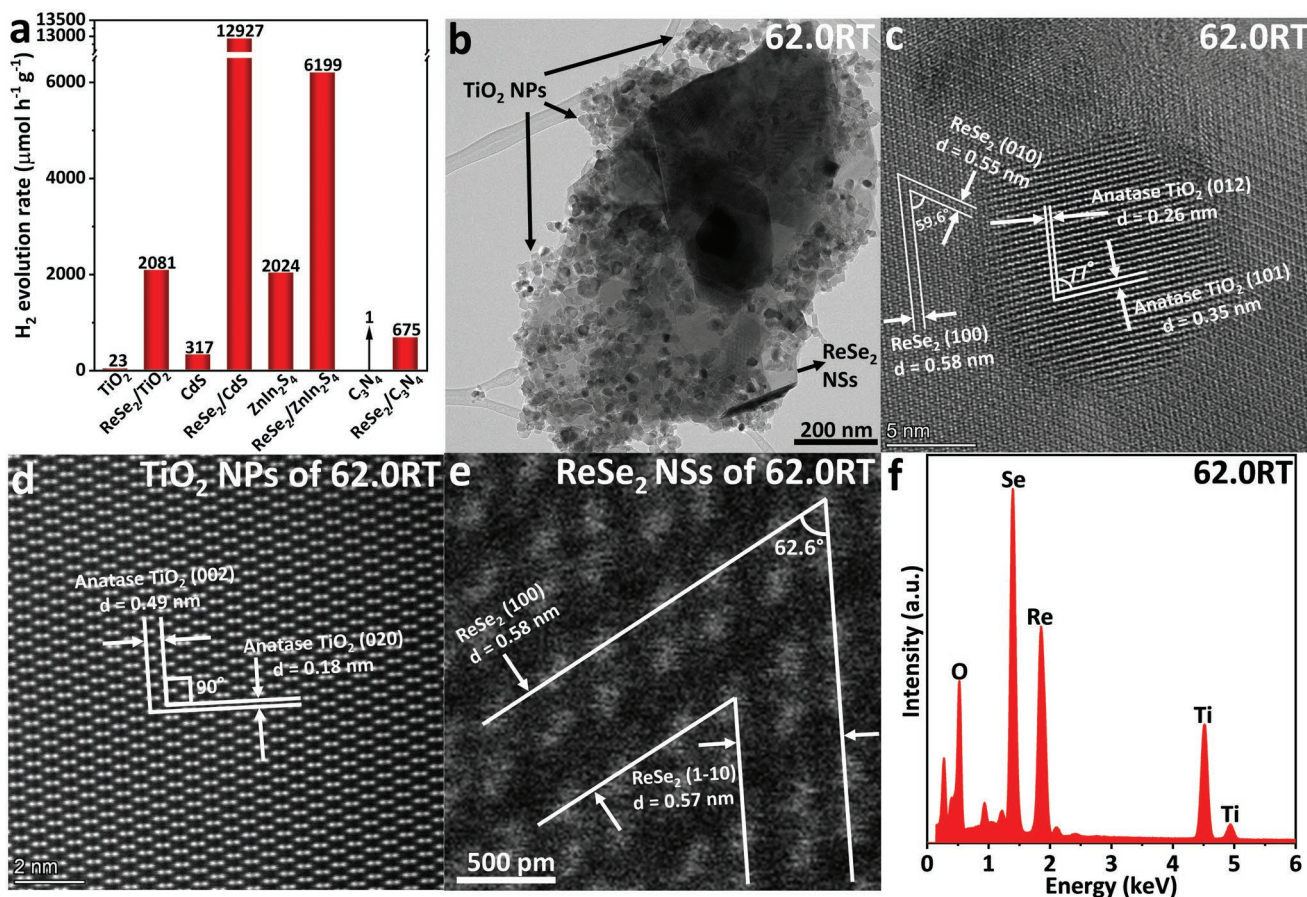


Figure 2. a) Photocatalytic H₂ evolution on TiO₂, ReSe₂/TiO₂, CdS, ReSe₂/CdS, ZnIn₂S₄, ReSe₂/ZnIn₂S₄, C₃N₄, and ReSe₂/C₃N₄ in ≈17.0 vol.% triethanolamine aqueous solution. TiO₂ and ReSe₂/TiO₂ were illuminated with xenon light without cut-off filter. CdS, ReSe₂/CdS, ZnIn₂S₄, ReSe₂/ZnIn₂S₄, C₃N₄, and ReSe₂/C₃N₄ were illuminated using visible light (λ > 400 nm). b) TEM and c) HRTEM images of 62.0RT. d) Atomic-resolution HAADF-STEM image of TiO₂ NPs in 62.0RT. e) Atomic-resolution low-dose HAADF-STEM image of ReSe₂ NSs in 62.0RT. f) EDX spectrum of 62.0RT. Brightness of Figure 2e was increased to highlight atoms of ReSe₂.

the appearance of triclinic-phase ReSe₂ peaks (JCPDS #52-0828) in the patterns for ReSe₂/TiO₂ composites confirms existence of ReSe₂ in ReSe₂/TiO₂ composites (Figure S19, Supporting Information).

Subsequently, a representative ReSe₂/TiO₂ composite, 62.0RT, was studied using TEM, HRTEM, atomic-resolution HAADF-STEM, EDX spectroscopy, electron energy loss spectroscopy (EELS), and EDX elemental mapping. The TEM image of 62.0RT (Figure 2b) indicates that numerous TiO₂ NPs are decorated on the ReSe₂ NSs surface. The HRTEM image of 62.0RT (Figure 2c) exhibits two lattice spacing values, 0.55 and 0.58 nm, and an angle of 59.6°, corresponding to the (010) and (100) facets of triclinic ReSe₂, respectively. Additionally, Figure 2c exhibits two inter-planar spacing values of 0.26 and 0.35 nm, and an angle of 77°, attributed to the (012) and (101) facets of anatase TiO₂, respectively. These are in accordance with the corresponding FFT pattern of 62.0RT (Figure S20, Supporting Information). The atomic-resolution HAADF-STEM image of anatase TiO₂ in 62.0RT (Figure 2d) exhibits the dumbbell structure for anatase TiO₂. Two lattice spacing values of 0.49 and 0.18 nm, together with an angle of 90° are seen in Figure 2d, which are attributed to the (002) and (020)

facets of anatase TiO₂, respectively. Additionally, Figure 2e exhibits two lattice spacing values of 0.58 and 0.57 nm with an angle of 62.6°, in accordance with the (100) and (1-10) facets of triclinic ReSe₂, respectively. Figure 2f suggests existence of Ti, O, Re, and Se elements, supporting the combination of TiO₂ and ReSe₂ in 62.0RT. Furthermore, the HAADF-STEM image of 62.0RT (Figure S21a, Supporting Information) and corresponding elemental mapping images of Re (Figure S21b, Supporting Information), Se (Figure S21c, Supporting Information), Ti (Figure S21d, Supporting Information), and O (Figure S21e, Supporting Information), all evidently support the loading of plentiful TiO₂ NPs on the surface of ReSe₂ NSs. The electron redistribution between ReSe₂ NSs and TiO₂ NPs in 62.0RT was studied utilizing various characterizations including, AFM-Kelvin probe force microscopy (KPFM), EELS, XPS, synchrotron-based XANES, and theoretical computation. An AFM image of 62.0RT (Figure S22a, Supporting Information) exhibits aggregation of TiO₂ NPs dispersed on the surface of ReSe₂ NS. The corresponding KPFM image (Figure S22b, Supporting Information) and potential profile (Figure S22c, Supporting Information) in darkness, confirm that the surface potential for TiO₂ NPs are greater than for ReSe₂ NS. This

finding indicates electron transfer from TiO₂ NPs to ReSe₂ NS after coupling in 62.0RT. Additionally, EELS Ti L edge (Figure 3a) and O K edge (Figure 3b) of the area located at the ReSe₂/TiO₂ interface in 62.0RT were obtained. As shown in Figure 3a,b, there is the apparent right shift of Ti L edge and O K edge for 62.0RT to higher energy loss direction, compared to those for 0.0RT. This finding also corroborates the electron transfer from TiO₂ NPs to ReSe₂ NSs at the interface area in 62.0RT.

Since the AFM-KPFM and EELS findings confirm only the local-area interfacial electron redistribution in 62.0RT, surface-sensitive XPS techniques were used to determine the overall electron redistribution at the surface of 62.0RT. As shown in Figure 3c,d, in comparison with Re 4f and Se 3d peaks of ReSe₂ NSs, those of 62.0RT exhibit apparent left shift of 0.7–1.0 eV to low binding energy direction. These findings strongly evidence the electron migration from TiO₂ NPs to ReSe₂ NSs at the surface of 62.0RT. The high-resolution XPS spectra of Ti 2p for 62.0RT (Figure 3e) exhibit no apparent peak shift compared with that for 0.0RT, due to the much higher content of TiO₂ (≈74.71 wt.%; Table S13, Supporting Information) than that of ReSe₂ (≈25.29 wt.%) in 62.0RT. However, the O 1s XPS peak for 62.0RT (Figure 3f) shows movement toward the high binding energy direction, in contrast to that for 0.0RT, supporting electron extraction from TiO₂ to ReSe₂ in 62.0RT. Because XPS can supply only information around the surface of 62.0RT, synchrotron-based XANES was used to determine electron redistribution in both the bulk and surface of 62.0RT. However, Figures S23 (Supporting Information) shows no apparent difference in the Se L edge, Ti L edge, and O K edge, when comparing those of 62.0RT with those of ReSe₂ NSs or 0.0RT. These findings confirm electron transfer occurs only around the surface of 62.0RT, especially the interface between ReSe₂ NSs and TiO₂ NPs in 62.0RT. Additionally, the work functions for ReSe₂ and TiO₂ considering the solvation effect were computed, respectively. ReSe₂ displays a greater work function ($\Phi = 3.946$ eV; Figure S24a, Supporting Information) compared with that for TiO₂ ($\Phi = 3.466$ eV; Figure S24b, Supporting Information), suggesting electron transfer from TiO₂ to ReSe₂ as these contact with each other. Importantly, this finding is further corroborated via the computed differential charge density map for ReSe₂/TiO₂ (Figure 3g). The apparent electron transfer from TiO₂ to ReSe₂ is confirmed with a Bader charge of $0.48 |e|$ (Figure 3g). Therefore, it is concluded that experimental characterizations and theoretical computation jointly disclose strong interface/surface electronic interaction in 62.0RT.

2.3. Photocatalytic Performances of ReSe₂/TiO₂ Composites

The photocatalytic H₂ evolution rates for 0.0RT, 6.0RT, 50.0RT, 62.0RT, 83.0RT, and ReSe₂ NSs were determined in ≈17 vol.% triethanolamine aqueous solution using xenon light (Figure 3h). TiO₂ (0.0RT) exhibits a very low efficiency of 23 μmol h⁻¹ g⁻¹. After coupling with a small amount of ReSe₂ NSs (≈3.17 wt.%; Table S13, Supporting Information), 6.0RT shows an obvious increase on photocatalytic H₂ evolution (555 μmol h⁻¹ g⁻¹; Figure 3h). Raising ReSe₂ content leads to a further boost on H₂ evolution to 975 μmol h⁻¹ g⁻¹. The highest H₂-evolution rate

(2081 μmol h⁻¹ g⁻¹) is achieved by 62.0RT. Hence, 62.0RT ranks as one of the most active TiO₂ based photocatalysts without any noble metal (Table S14, Supporting Information). However, further increasing ReSe₂ results in a reduction on H₂ evolution to 1368 μmol h⁻¹ g⁻¹. This finding is attributed to blocked surface active sites and shielded light absorption caused by redundant ReSe₂ NSs in 83.0RT. Additionally, ReSe₂ NSs exhibits a very low photocatalytic H₂ evolution (1 μmol h⁻¹ g⁻¹). The explanation is that the photogenerated holes with weak oxidation ability in ReSe₂ NSs cannot be efficiently consumed by the electron donor, triethanolamine, thereby leading to rapid recombination of photo-generated electrons and holes.

Robustness of 62.0RT on photocatalytic H₂ evolution was also assessed. As shown in Figure S25a (Supporting Information), after 3 h photocatalytic reaction, 62.0RT reserved ≈53.8% of the H₂ evolution in the first hour. This finding confirms acceptable stability of 62.0RT. To investigate the reduced photocatalytic efficiency of 62.0RT, a range of characterizations were carried out. 62.0RT after the 3 h reaction was denoted as 62.0RT-A. A TEM image of 62.0RT-A (Figure S25b, Supporting Information) shows no apparent difference in morphologies of TiO₂ NPs and ReSe₂ NSs compared with those for 62.0RT (Figure 2b). The EDX spectrum for 62.0RT-A (Figure S25c, Supporting Information) indicates existence of Re, Se, Ti, and O elements, in accordance with those for 62.0RT before reaction (Figure 2f). Thus, atomic-resolution HAADF-STEM was used to further explore 62.0RT-A. Some amorphous region at the edge of ReSe₂ NSs in 62.0RT-A can be seen in Figure S25d,e (Supporting Information), suggesting that the photo- and/or chemical-corrosion can result in amorphization of active edge sites for ReSe₂ NSs. This can lead to activity reduction following the 3 h reaction of 62.0RT. HER electrochemical stability of 62.0RT (Figure S26, Supporting Information) displays the excellent HER stability of 62.0RT and its robustness in the reduction and alkaline environments. This finding reveals that the instability of 62.0RT could arise from self-oxidation of ReSe₂ NSs by photo-generated holes.

2.4. Origin of High Performance for ReSe₂/TiO₂ Composite

To determine the origin of significant raise on photocatalytic efficiency, both state-of-art characterizations and theoretical computation were conducted for the most active ReSe₂/TiO₂ nanocomposite (62.0RT). Since charge separation/transfer efficiency is of central importance for photocatalytic H₂ evolution, a series of characterizations, including steady-state/transient-state photoluminescence (PL) spectroscopy, steady-state/transient-state surface photo-voltage (SPV) spectroscopy, in situ XPS, and transient photocurrent density (TPC) measurement, were adopted.

The steady-state photoluminescence (PL) spectra for 0.0RT and 62.0RT (Figure S27a, Supporting Information) exhibit that the PL intensity of 62.0RT is much lower than that for 0.0RT. This confirms that the charge carrier recombination is significantly reduced for 62.0RT compared with that for 0.0RT. The transient-state PL spectra for 0.0RT and 62.0RT are shown in Figure S27b (Supporting Information). 62.0RT exhibits longer fitted charge carrier lifetimes ($\tau_1 = 0.171$ ns, $\tau_2 = 3.850$ ns and

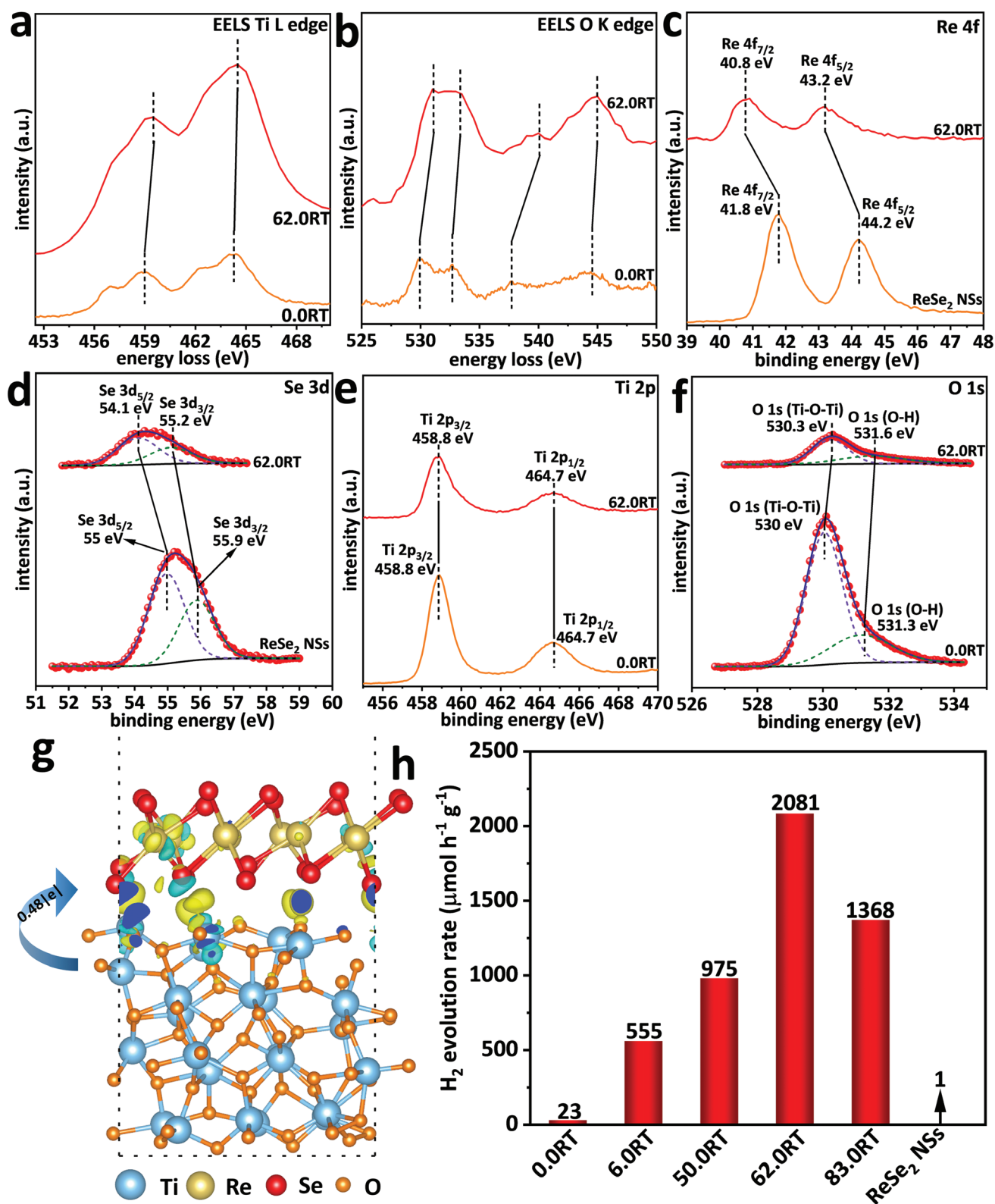


Figure 3. Electron energy loss spectroscopy (EELS) spectra of a) Ti L edge and b) O K edge for 0.0RT and 62.0RT. High-resolution XPS spectra of c) Re 4f and d) Se 3d for ReSe₂ NSs and 62.0RT. High-resolution XPS spectra of e) Ti 2p and f) O 1s for 0.0RT and 62.0RT. g) Computed differential charge density map at interface of ReSe₂ (002) facet/TiO₂ (111) facet system considering solvation effect in 17 vol.% triethanolamine aqueous solution. h) Photocatalytic H₂ evolution of 0.0RT, 6.0RT, 50.0RT, 62.0RT, 83.0RT and ReSe₂ NSs in ≈17 vol.% triethanolamine aqueous solution using xenon light.

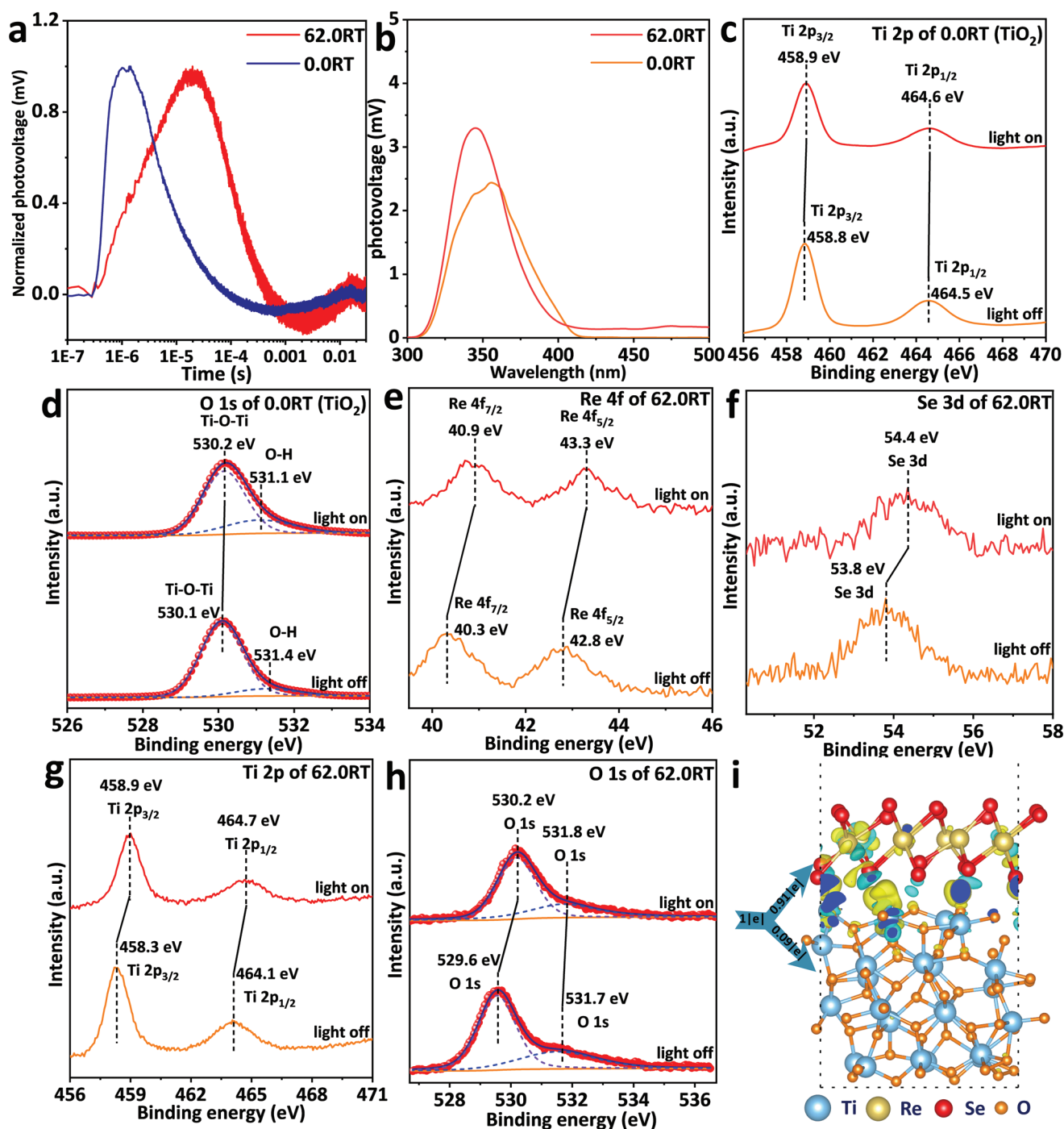


Figure 4. a) Normalized transient-state surface photovoltage spectra of 0.0RT and 62.0RT. b) Steady-state surface photovoltage spectra of 0.0RT and 62.0RT. High-resolution XPS spectra of c) Ti 2p and d) O 1s for 0.0RT (TiO_2) with light, respectively, on and off. High-resolution XPS spectra of e) Re 4f, f) Se 3d, g) Ti 2p, and h) O 1s for 62.0RT with light, respectively, on and off. i) Differential charge density map at the interface of $\text{ReSe}_2/\text{TiO}_2$ system with extra one electron considering solvation effect in 17 vol.% triethanolamine aqueous solution.

intensity-averaged $\tau_{\text{ave}} = 0.313$ ns), than those for 0.0RT ($\tau_1 = 0.167$ ns, $\tau_2 = 3.631$ ns, and $\tau_{\text{ave}} = 0.260$ ns), suggesting boosted separation/transfer of photo-generated electrons and holes in 62.0RT compared with that in 0.0RT.

Steady-state/transient-state PL spectroscopy provides information on the charge separation/transfer both on the surface

and in the bulk of 62.0RT. However, given that photocatalytic reactions generally occur on the surface of 62.0RT, advanced characterizations were applied to assess the photo-generated electron-hole separation/transportation on the surface. These include steady-state/transient-state SPV spectroscopy and in situ XPS. The normalized transient-state SPV spectra for

0.0RT and 62.0RT (Figure 4a) show that the transient SPV signal for 62.0RT decays significantly slower than that for 0.0RT. This finding confirms that the charge carrier separation and transfer efficiency in 62.0RT is significantly boosted in comparison with that for 0.0RT. This is also supported by the reported reference.^[58] The positive signal for SPV evidences that more photo-generated holes migrate to the surface compared with photo-generated electrons. A small negative SPV signal is observed on 62.0RT at the time scale of $\approx 0.001\text{--}0.01$ s, suggesting that more photo-induced electrons than holes are on the surface of 62.0RT at this time scale. Moreover, the steady-state SPV intensity for 62.0RT is higher than that for 0.0RT (Figure 4b), suggesting that coupling of ReSe₂ NSs and TiO₂ obviously boosts migration of more photo-generated holes to the surfaces of TiO₂ and ReSe₂ NSs in 62.0RT. Because steady-state/transient-state SPV findings cannot disclose separation/transfer of photo-generated electrons/holes on the surface of different components (TiO₂ NPs or ReSe₂ NSs) in 62.0RT, in situ XPS spectra were used to understand the dissociation/transfer of photo-induced electrons/holes on the surface of TiO₂ NPs and ReSe₂ NSs, respectively, in 62.0RT. High-resolution XPS spectra of Re 4f and Se 3d for ReSe₂ NSs with/without light illumination are shown in Figure S28a,b (Supporting Information), respectively. Both Re 4f and Se 3d peaks for ReSe₂ NSs exhibit left movement to low binding energy direction following light illumination, indicating that more photogenerated electrons than holes transfer to the surface of ReSe₂ NSs after light excitation. Additionally, the high-resolution XPS spectra for Ti 2p (Figure 4c) and O 1s (Figure 4d) peaks for 0.0RT (TiO₂) show right shift towards high binding energy direction with light illumination, in contrast to those without light illumination. These findings confirm that more photogenerated holes than electrons transfer to the surface of TiO₂ NPs with light excitation. Additionally, with light illumination all high-resolution XPS spectra of Re 4f, Se 3d, Ti 2p, and O 1s peaks for 62.0RT (Figure 4e–h), shift to the higher binding energy direction, in contrast to those without light irradiation. To seek the reason for this finding, the hetero-junction type for 62.0RT was confirmed. The MS plot for 0.0RT (Figure S29a, Supporting Information) shows the E_F potential of 0.0RT (-0.57 V vs Ag/AgCl), equivalent to 0.06 V vs SHE. Based on the XPS VB spectrum of 0.0RT (Figure S29b, Supporting Information), the VB potential for 0.0RT is 2.54 V versus SHE. Therefore, the CB potential for 0.0RT is -0.66 V versus SHE based on the bandgap for 0.0RT ($E = 3.20$ eV; Figure S30, Supporting Information). Thus, there exists a type I hetero-junction between TiO₂ NPs and ReSe₂ NSs in 62.0RT (Figure S31, Supporting Information). With light excitation, the photo-generated electrons and holes would transfer from the CB and VB of TiO₂ NPs to the CB and VB of ReSe₂ NSs, respectively. However, the huge potential difference between VB edges of TiO₂ NPs and ReSe₂ NSs (1.76 V) would significantly boosts hole transport from bulk TiO₂ NPs onto the surfaces of both TiO₂ NPs and ReSe₂ NSs. In contrast, the much lower potential difference (0.37 V) between the CB edges of TiO₂ NPs and ReSe₂ NSs cannot equally boost efficient transfer of photo-generated electrons from bulk TiO₂ NPs to the surfaces of both TiO₂ NPs and ReSe₂ NSs. Therefore, more photo-generated holes than electrons accumulate on the surface of both TiO₂ NPs and ReSe₂ NSs, resulting in the shift of all

XPS peaks to the higher binding energy direction (Figure 4e–h). This is in accordance with the SPV findings (Figures 4a,b). In addition, Figure S32a (Supporting Information) displays raised TPC density for 62.0RT over that for 0.0RT, thus confirming boosted photo-excited electron–hole separation/migration in 62.0RT. Furthermore, the charge dissociation/transport in ReSe₂/TiO₂ was explored using theoretical computation. Redistribution for photo-induced electron in ReSe₂/TiO₂ was simulated through adding one electron to ReSe₂/TiO₂ system. The differential charge density analysis (Figure 4i) shows that $0.91|e|$ transfers to ReSe₂ whilst $0.09|e|$ migrates to TiO₂, confirming the stronger electron-accepting ability of ReSe₂ compared to that of TiO₂ with light excitation. Therefore, photo-induced electron would transfer from TiO₂ to ReSe₂ in 62.0RT, in accordance with the formation of type I heterojunction for ReSe₂/TiO₂ composite (Figure S31, Supporting Information).

The light harvesting ability of 62.0RT was investigated by UV–vis diffuse reflectance spectra of all samples (Figure S30, Supporting Information). Apparent absorption increases in the range of $\approx 400\text{--}800$ nm is observed for ReSe₂/TiO₂ hybrids in comparison with bare TiO₂ (Figure S30, Supporting Information). This is because of strong light absorption by ReSe₂ NSs with small bandgap ($E = 1.07$ eV). To confirm whether the increased absorption by ReSe₂ NSs could result in boosted photocatalytic H₂ evolution, a 740-nm light emitting diode (LED) was used to illuminate 62.0RT at the same reaction conditions. However, negligible activity was observed (Figure S32b, Supporting Information). This result reveals that although obvious increases are observed at $\approx 400\text{--}800$ nm for all the hybridized samples, these increases cause negligible contribution to boosted activities.

Nitrogen (N₂) sorption isotherms of 0.0RT, 6.0RT, 50.0RT, 62.0RT, and 83.0RT are demonstrated in Figure S33 (Supporting Information). Compared with the N₂ sorption isotherm for 0.0RT, N₂ sorption isotherms for 6.0RT, 50.0RT, 62.0RT, and 83.0RT shift downward in the relative-pressure range of $0.05\text{--}0.9$ and upward in the range of $\approx 0.9\text{--}1.0$ (Figure S33, Supporting Information), confirming reduced numbers of small mesopores and increased numbers of large mesopores/macropores, respectively. These are also reflected in the pore size distribution curves for all the samples (Figure S33 insets, Supporting Information). Since the Brunauer–Emmett–Teller (BET) surface area (S_{BET}) is mainly contributed via existence of mesopores other than macropores, it is not surprising that S_{BET} values for ReSe₂/TiO₂ composites are reduced gradually with increasing contents of ReSe₂ NSs (Table S13, Supporting Information). The specific photocatalytic H₂ evolution activity based on S_{BET} are displayed in Table S13 (Supporting Information). As shown in Table S13 (Supporting Information), with increasing contents of ReSe₂, specific photocatalytic activity is raised from $0.42 \mu\text{mol h}^{-1} \text{m}^{-2}$ (0.0RT) to $51.27 \mu\text{mol h}^{-1} \text{m}^{-2}$ (83.0RT). This is because that increasing ReSe₂ NSs amounts result in raised numbers of atomic-level active sites for HER and reduced S_{BET} values. These findings confirm that S_{BET} value is not the major factor impacting activity of ReSe₂/TiO₂ composite. Electrochemical HER was tested for 0.0RT and 62.0RT. As shown in Figure S34a (Supporting Information), HER activity of 62.0RT is boosted compared with 0.0RT following coupling of ReSe₂ NSs and TiO₂ NPs in alkaline solution. This evidences the

existence of numerous edge active sites on ReSe₂ NSs to boost H₂ evolution on 62.0RT. Additionally, theoretical computations were carried out to acquire ΔG_{H^*} on the sites of ReSe₂ basal plane in ReSe₂/TiO₂ (Figure S34b,c, Supporting Information). All ReSe₂ basal sites in ReSe₂/TiO₂ display reduced values for ΔG_{H^*} compared with basal sites in ReSe₂ alone, attributed to the strong electronic coupling between ReSe₂ and TiO₂. In addition, Se4 site in ReSe₂/TiO₂ exhibits a significantly reduced $|\Delta G_{H^*}|$ value of 0.12 eV (Table S15, Supporting Information) in contrast to Se4 in ReSe₂ alone (Table S2, Supporting Information). It is concluded therefore that ReSe₂ basal plane Se4 site in ReSe₂/TiO₂ serves as the highly-active HER site.

Based on the results from combined experiment and theoretical computation, we hypothesized a novel photocatalytic mechanism (Figure S35, Supporting Information). As shown in Figure S31 (Supporting Information), TiO₂ NPs and ReSe₂ NSs form a type I (straddling type) heterojunction, with CB and VB potential differences of 0.37 and 1.76 V, respectively. From the view of thermodynamics, the much greater VB potential difference (1.76 V) compared with CB potential difference (0.37 V) would boost much faster transport of photo-induced holes than electrons from the bulk/surface of TiO₂ across the interface to the bulk/surface of ReSe₂. Actually, with xenon light illumination, the photo-generated holes in the bulk of TiO₂ NPs migrate to the surface, most of which are rapidly captured and scavenged by the sacrificial electron donor (triethanolamine); while a small number of photo-generated holes transfer to ReSe₂ NSs (Figure S35, Supporting Information). The photo-induced electrons in the CB of TiO₂ NPs transfer to the CB of ReSe₂ NSs, and reduce protons to evolve H₂ gas at the atomic-level edge/basal plane active Re/Se sites and activated basal Se sites (Figure S35, Supporting Information). Because the photo-generated electrons and holes in ReSe₂ cannot contribute to photocatalytic H₂ evolution (Figure S32b, Supporting Information), the photo-excitation of ReSe₂ is not shown in Figure S35 (Supporting Information).

2.5. ReSe₂ NSs as Universal Platform

To confirm that atomic-level regulated ReSe₂ NSs can function as a universal platform to boost photocatalytic H₂ evolution on various semiconductor photocatalysts, a range of experiments were conducted to confirm the generality of ReSe₂ NSs. As shown in Figure 2a, photocatalytic H₂ evolution of ReSe₂/CdS (12927 $\mu\text{mol h}^{-1} \text{g}^{-1}$), ReSe₂/ZnIn₂S₄ (6199 $\mu\text{mol h}^{-1} \text{g}^{-1}$), or ReSe₂/C₃N₄ (675 $\mu\text{mol h}^{-1} \text{g}^{-1}$) is significantly greater than that of CdS (317 $\mu\text{mol h}^{-1} \text{g}^{-1}$), ZnIn₂S₄ (2024 $\mu\text{mol h}^{-1} \text{g}^{-1}$), or C₃N₄ (1 $\mu\text{mol h}^{-1} \text{g}^{-1}$). ReSe₂/CdS (Figure 5a; Table S16, Supporting Information), ReSe₂/ZnIn₂S₄ (Figure 5b; Table S17, Supporting Information), and ReSe₂/C₃N₄ (Figure 5c; Table S18, Supporting Information) all rank among one of the most efficient CdS, ZnIn₂S₄ and C₃N₄-based photocatalysts, respectively, in the absence of any noble metal. Therefore, the highly active ReSe₂/CdS, ReSe₂/ZnIn₂S₄ and ReSe₂/C₃N₄ were comprehensively characterized. The XRD patterns for ReSe₂/CdS, ReSe₂/ZnIn₂S₄, and ReSe₂/C₃N₄ are given in Figure S36a–c (Supporting Information), respectively. The (001) peaks of triclinic ReSe₂ (JCPDS #52-0828) are observed in Figure S36a–c (Supporting Information), confirming the

coupling of ReSe₂ NSs with CdS, ZnIn₂S₄, and C₃N₄, respectively. Additionally, the TEM images (Figure S37a–c, Supporting Information), EDX spectra (Figure S37d–f, Supporting Information), HRTEM images (Figure 5d–f) and corresponding FFT patterns (Figure S38a–c, Supporting Information) for ReSe₂/CdS, ReSe₂/ZnIn₂S₄ and ReSe₂/C₃N₄ also corroborate coupling of ReSe₂ NSs with CdS NPs, ZnIn₂S₄ NSs, and C₃N₄, respectively. The HAADF-STEM images and corresponding elemental mapping images for ReSe₂/CdS (Figure S39a–e, Supporting Information), ReSe₂/ZnIn₂S₄ (Figure S39f–k, Supporting Information), and ReSe₂/C₃N₄ (Figure S39i–p, Supporting Information) further confirm the coupling between ReSe₂ NSs and CdS NPs, ZnIn₂S₄ NSs, or C₃N₄. Surface-sensitive XPS technique was used to reveal the interfacial electronic coupling in ReSe₂/CdS, ReSe₂/ZnIn₂S₄, and ReSe₂/C₃N₄. The high-resolution XPS spectra for ReSe₂/CdS (Figure S40a–d, Supporting Information), ReSe₂/ZnIn₂S₄ (Figure S40e–h, Supporting Information), and ReSe₂/C₃N₄ (Figure S40i–l, Supporting Information) exhibit evident peak shift, strongly evidencing electron extraction to ReSe₂ from CdS, ZnIn₂S₄, or C₃N₄. Moreover, the UV–vis diffuse reflectance spectra for ReSe₂/CdS (Figure S41a, Supporting Information), ReSe₂/ZnIn₂S₄ (Figure S41b, Supporting Information), and ReSe₂/C₃N₄ (Figure S41c, Supporting Information) demonstrate the increase on light absorption up to 800 nm, attributed to integration of ReSe₂ with a narrow band gap ($E = 1.07$ eV). To confirm whether this increased absorption can boost activity, a 740-nm LED, instead of xenon light, was used to excite ReSe₂ only. Negligible efficiency is observed for ReSe₂/CdS, ReSe₂/ZnIn₂S₄, or ReSe₂/C₃N₄ in the same reaction conditions (Figure S41d–f, Supporting Information), indicating that no efficiency boost is induced by light absorption of ReSe₂ in these composites. The charge dissociation/transfer in these composites was assessed. All steady-state PL (Figure S42a–c, Supporting Information), TSPL (Figure 5g–i) and TPC density measurement (Figure S42d–f, Supporting Information) suggest the more efficient photo-generated electron/hole dissociation/transportation in ReSe₂/CdS, ReSe₂/ZnIn₂S₄ and ReSe₂/C₃N₄, compared with bare CdS, ZnIn₂S₄ and C₃N₄, respectively. Additionally, HER activities for ReSe₂/CdS, ReSe₂/ZnIn₂S₄, and ReSe₂/C₃N₄ are obviously raised, in contrast with those for bare CdS, ZnIn₂S₄, and C₃N₄, respectively (Figure 5j–l). These findings confirm that the existence of ReSe₂ NSs with numerous active sites obviously accelerate HER. HER stabilities for ReSe₂/CdS, ReSe₂/ZnIn₂S₄ and ReSe₂/C₃N₄ were tested, and findings (Figure S43a–c, Supporting Information) confirm stable HER for >20 h. This suggest the robust HER activities for ReSe₂/CdS, ReSe₂/ZnIn₂S₄ and ReSe₂/C₃N₄ in alkaline solution with reduction condition. A slightly reduced HER current density for ReSe₂/C₃N₄ is observed in Figure S43c (Supporting Information), attributed to the less stability of C₃N₄ compared to CdS or ZnIn₂S₄ in the 20 h HER. Therefore, we validate the universality of ReSe₂ to boost the activities on different semiconductor photocatalysts, including CdS, ZnIn₂S₄, and C₃N₄.

3. Conclusion

Atomic-level and controllably engineered ReSe₂ nanosheets (NSs) are used as the versatile platform to combine with

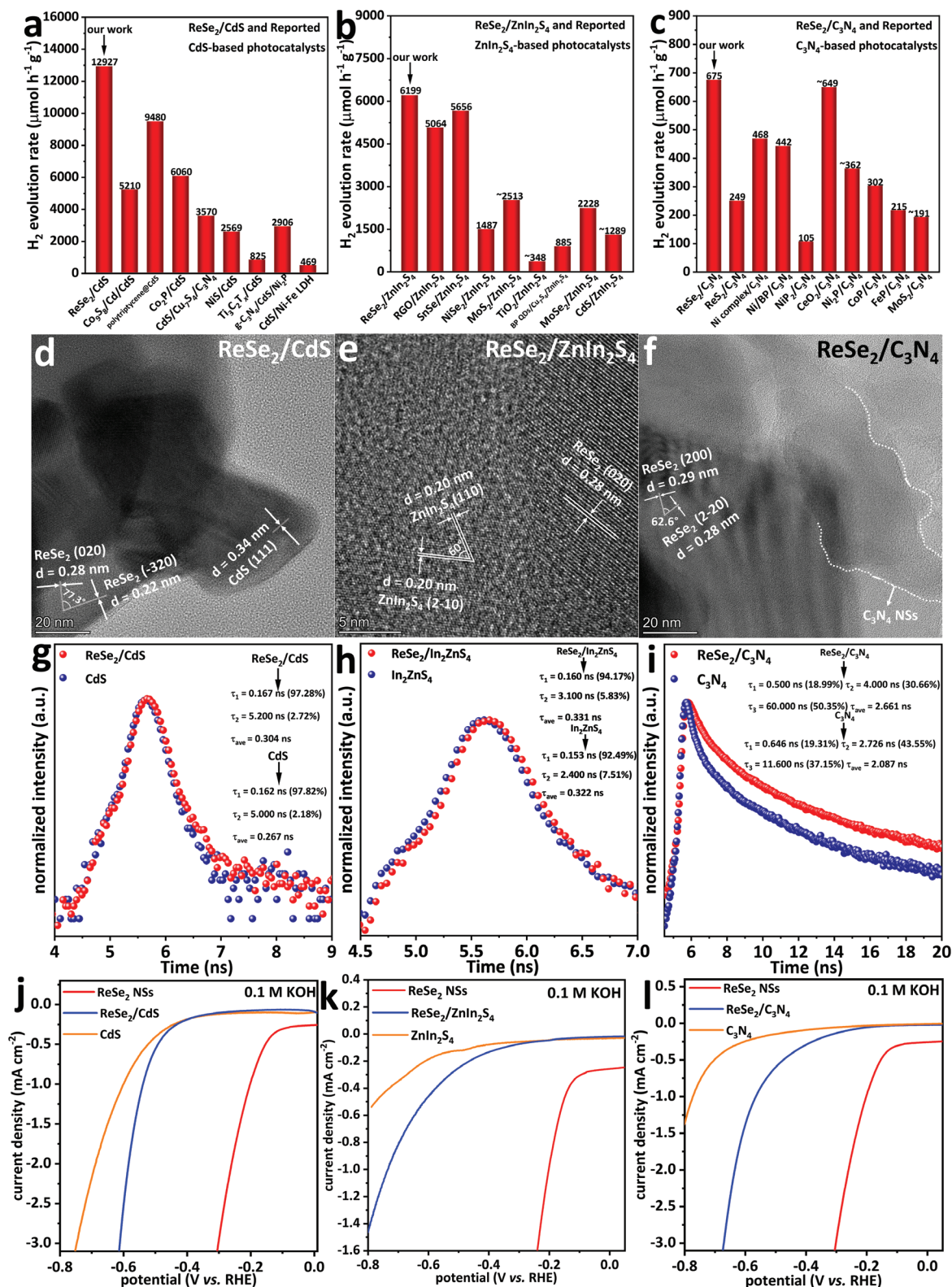


Figure 5. photocatalytic H_2 evolution for reported noble-metal-free a) CdS-based, b) ZnIn_2S_4 -based, and c) C_3N_4 -based photocatalysts compared with the corresponding ReSe_2 based photocatalysts in our work, respectively. HRTEM images of d) ReSe_2/CdS nanocomposite, e) $\text{ReSe}_2/\text{ZnIn}_2\text{S}_4$ nanocomposite, and f) $\text{ReSe}_2/\text{C}_3\text{N}_4$ nanocomposite. Transient-state PL spectra for g) CdS and ReSe_2/CdS , h) ZnIn_2S_4 and $\text{ReSe}_2/\text{ZnIn}_2\text{S}_4$, and i) C_3N_4 and $\text{ReSe}_2/\text{C}_3\text{N}_4$. Insets in (g–i) show the fitted and averaged charge carrier lifetimes. HER activities of j) CdS and ReSe_2/CdS , k) ZnIn_2S_4 and $\text{ReSe}_2/\text{ZnIn}_2\text{S}_4$ and l) C_3N_4 and $\text{ReSe}_2/\text{C}_3\text{N}_4$ in 0.1 M KOH aqueous solution.

different semiconductor photocatalysts, including TiO₂, CdS, ZnIn₂S₄, and C₃N₄, to significantly boost photocatalytic H₂ evolution. Among them, the highest enhancement factor of ≈9048% is achieved on TiO₂ nanoparticles (NPs) loaded ReSe₂ NSs, with a photocatalytic H₂ evolution rate of 2081 μmol h⁻¹ g⁻¹. This ReSe₂/TiO₂ system is investigated by both theoretical calculations and state-of-art characterizations. Both theoretical calculations and experimental results support that the distinct electronic interaction between the TiO₂ NPs and ReSe₂ NSs boost the efficient separation/migration of photo-generated electrons/holes; while the abundant Re/Se active sites at the defected edge/basal plane and activated Se site in the basal plane of ReSe₂ NSs greatly advance H₂ evolution. This work not only demonstrates the atomic-level engineering of ReSe₂ NSs as a universal platform to significantly raise photocatalytic H₂ evolution, but also pave avenues to the atomic-level design and synthesis of materials for energy applications.

4. Experimental Section

Experimental details can be found in the Supporting Information.

Supporting Information

Supporting Information is available from the Wiley Online Library or from the author.

Acknowledgements

J.R., L.C., and D.W. contributed equally to this work. The authors gratefully acknowledge financial support from the Australian Research Council (ARC) through the Discovery Project programs (FL170100154, DE200100629, DP22102596) and Linkage Project (LP210301397). The authors acknowledge the Australian Synchrotron (AS) for the XANES measurement at the soft X-ray spectroscopy beamline. The authors also acknowledge Hongping Zhang for assistance on theoretical computations, as well as Sijia Fu, Bingquan Xia, Jieqiong Shan, Yunling Jiang, and Elhussein Mohamed Mahmoud Hashem for assistance on experiments.

Open access publishing facilitated by The University of Adelaide, as part of the Wiley - The University of Adelaide agreement via the Council of Australian University Librarians.

Conflict of Interest

The authors declare no conflict of interest.

Data Availability Statement

The data that support the findings of this study are available from the corresponding author upon reasonable request.

Keywords

atomic-level active sites, defected ReSe₂ nanosheets, interface engineering, photocatalytic H₂ evolution

Received: November 3, 2022
Revised: February 7, 2023
Published online: March 24, 2023

- [1] A. Fujishima, K. Honda, *Nature* **1972**, 238, 37.
- [2] H. Nishiyama, T. Yamada, M. Nakabayashi, Y. Maehara, M. Yamagu-chi, Y. Kuromiya, Y. Nagatsuma, H. Tokudome, S. Akiyama, T. Watanabe, R. Narushima, S. Okunaka, N. Shibata, T. Takata, T. Hisatomi, K. Domen, *Nature* **2021**, 598, 304.
- [3] X. Ren, F. Liu, Q. Wang, H. Song, S. Luo, S. Li, G. Yang, B. Deng, Z. Huang, X.-S. Wang, L. Shi, J. Ye, *Appl. Catal. B-Environ.* **2022**, 303, 120887.
- [4] D. Gao, J. Xu, L. Wang, B. Zhu, H. Yu, J. Yu, *Adv. Mater.* **2022**, 34, 2108475.
- [5] Y.-J. Yuan, N. Lu, L. Bao, R. Tang, F.-G. Zhang, J. Guan, H.-D. Wang, Q.-Y. Liu, Q. Cheng, Z.-T. Yu, Z. Zou, *ACS Nano* **2022**, 16, 12174.
- [6] P. Dong, Y. Wang, A. Zhang, T. Cheng, X. Xi, J. Zhang, *ACS Catal.* **2021**, 11, 13266.
- [7] C. Zhang, H. Wang, H. Yu, K. Yi, W. Zhang, X. Yuan, J. Huang, Y. Deng, G. Zeng, *Adv. Energy Mater.* **2022**, 12, 2200875.
- [8] V. Andrei, G. M. Ucoski, C. Pornrunroj, C. Uswachoke, Q. Wang, D. S. Achilleos, H. Kasap, K. P. Sokol, R. A. Jagt, H. Lu, T. Lawson, A. Wagner, S. D. Pike, D. S. Wright, R. L. Z. Hoye, *Nature* **2022**, 608, 518.
- [9] Y. Qi, J. Zhang, Y. Kong, Y. Zhao, S. Chen, D. Li, W. Liu, Y. Chen, T. Xie, J. Cui, C. Li, K. Domen, F. Zhang, *Nat. Commun.* **2022**, 13, 484.
- [10] J. Ran, H. Zhang, J. Qu, J. Shan, K. Davey, J. M. Cairney, L. Jing, S.-Z. Qiao, *Small* **2021**, 17, 2100296.
- [11] D. Zhao, Y. Wang, C.-L. Dong, Y.-C. Huang, J. Chen, F. Xue, S. Shen, L. Guo, *Nat. Energy* **2021**, 6, 388.
- [12] Z.-A. Lan, M. Wu, Z. Fang, Y. Zhang, X. Chen, G. Zhang, X. Wang, *Angew. Chem., Int. Ed.* **2022**, 61, e202201482.
- [13] R. Chen, Y. Wang, Y. Ma, A. Mal, X.-Y. Gao, L. Gao, L. Qiao, X.-B. Li, L.-Z. Wu, C. Wang, *Nat. Commun.* **2021**, 12, 1354.
- [14] F. Wang, Y. Jiang, A. Gautam, Y. Li, R. Amal, *ACS Catal.* **2014**, 4, 1451.
- [15] J. Guan, T. Pal, K. Kamiya, N. Fukui, H. Maeda, T. Sato, H. Suzuki, O. Tomita, H. Nishihara, R. Abe, R. Sakamoto, *ACS Catal.* **2022**, 12, 3881.
- [16] B. Tian, Y. Wu, G. Lu, *Appl. Catal. B-Environ.* **2021**, 280, 119410.
- [17] S. Nishioka, T. Oshima, S. Hirai, D. Saito, K. Hojo, T. E. Mallouk, K. Maeda, *ACS Catal.* **2021**, 11, 659.
- [18] Y. Bai, K. Nakagawa, A. J. Cowan, C. M. Aitchison, Y. Yamaguchi, M. A. Zwijnenburg, A. Kudo, R. S. Sprick, A. I. Cooper, *J. Mater. Chem. A* **2020**, 8, 16283.
- [19] J. Dong, W. Fang, H. Yuan, W. Xia, X. Zeng, W. Shangguan, *ACS Appl. Energy Mater.* **2022**, 5, 4893.
- [20] G. Zhi, S. Ling, S.-F. Ng, W.-J. Ong, *Adv. Funct. Mater.* **2022**, 32, 2111875.
- [21] J. Ran, H. Zhang, S. Fu, M. Jaroniec, J. Shan, B. Xia, Y. Qu, J. Qu, S. Chen, L. Song, J. M. Cairney, L. Jing, S.-Z. Qiao, *Nat. Commun.* **2022**, 13, 4600.
- [22] Z. Wang, F. Yang, T. Ding, M.-H. Lee, Q. Yang, *J. Alloys Compd.* **2022**, 918, 165786.
- [23] J. Ran, H. Zhang, J. Qu, J. Shan, S. Chen, F. Yang, R. Zheng, J. Cairney, L. Song, L. Jing, S.-Z. Qiao, *ACS Mater. Lett.* **2020**, 2, 1484.
- [24] Y. Cao, S. Chen, Q. Luo, H. Yan, Y. Lin, W. Liu, L. Cao, J. Lu, J. Yang, T. Yao, S. Wei, *Angew. Chem., Int. Ed.* **2022**, 61, e202201482.
- [25] Y. Chen, S. Ji, W. Sun, Y. Lei, Q. Wang, A. Li, W. Chen, G. Zhou, Z. Zhang, Y. Wang, L. Zheng, Q. Zhang, L. Gu, X. Han, D. Wang, Y. Li, *Angew. Chem., Int. Ed.* **2020**, 59, 1295.

- [26] L. Su, P. Wang, J. Wang, D. Zhang, H. Wang, Y. Li, S. Zhan, J. Gong, *Adv. Funct. Mater.* **2021**, *31*, 2104343.
- [27] S. Hejazi, S. Mohajernia, B. Osuagwu, G. Zoppellaro, P. Andryskova, O. Tomanec, S. Kment, R. Zbořil, P. Schmuki, *Adv. Mater.* **2020**, *32*, 1908505.
- [28] R. Feng, K. Wan, X. Sui, N. Zhao, H. Li, W. Lei, J. Yu, X. Liu, X. Shi, M. Zhai, G. Liu, H. Wang, L. Zheng, M. Liu, *Nano Today* **2021**, *37*, 101080.
- [29] R. Zeng, C. Cheng, F. Xing, Y. Zou, K. Ding, C. Huang, *Appl. Catal. B-Environ.* **2022**, *316*, 121680.
- [30] F. Chen, T. Ma, T. Zhang, Y. Zhang, H. Huang, *Adv. Mater.* **2021**, *33*, 2005256.
- [31] X. Shi, Y. Huang, Y. Bo, D. Duan, Z. Wang, J. Cao, G. Zhu, W. Ho, L. Wang, T. Huang, Y. Xiong, *Angew. Chem., Int. Ed.* **2022**, *61*, e202203.
- [32] J. Di, C. Chen, C. Zhu, R. Long, H. Chen, X. Cao, J. Xiong, Y. Weng, L. Song, S. Li, H. Li, Y. Xiong, Z. Liu, *Adv. Energy Mater.* **2021**, *11*, 2102389.
- [33] I. S. Kwon, I. H. Kwak, S. Ju, S. Kang, S. Han, Y. C. Park, J. Park, J. Park, *ACS Nano* **2020**, *14*, 12184.
- [34] R. Wang, J. Han, P. Xu, T. Gao, J. Zhong, X. Wang, X. Zhang, Z. Li, L. Xu, B. Song, *Adv. Sci.* **2020**, *7*, 2000216.
- [35] S. Jiang, Z. Zhang, N. Zhang, Y. Huan, Y. Gong, M. Sun, J. Shi, C. Xie, P. Yang, Q. Fang, H. Li, L. Tong, D. Xie, L. Gu, P. Liu, Y. Zhang, *Nano Res.* **2018**, *11*, 1787.
- [36] J. Li, Y. Liu, C. Liu, W. Huang, Y. Zhang, M. Wang, Z. Hou, X. Wang, M. Jin, G. Zhou, X. Gao, Z. Zhang, J. Liu, *Chem. Commun.* **2020**, *56*, 305.
- [37] F. Qi, X. Wang, B. Zheng, Y. Chen, B. Yu, J. Zhou, J. He, P. Li, W. Zhang, Y. Li, *Electrochim. Acta* **2017**, *224*, 593.
- [38] F. Sultana, M. Mushtaq, T. Ferdous, J. Wang, M. Lin, A. Zaman, K. Althubeiti, M. Aljohanig, Q. Yang, *New J. Chem.* **2022**, *46*, 14894.
- [39] M. Zhuang, G.-L. Xu, L.-Y. Gan, Y. Dou, C.-J. Sun, X. Ou, Y. Xie, Z. Liu, Y. Cai, Y. Ding, I. H. Abidi, A. Tyagi, K. Amine, Z. Luo, *Nano Energy* **2019**, *58*, 660.
- [40] Y. Yan, S. Xu, H. Li, N. C. S. Selvam, J. Y. Lee, H. Lee, P. J. Yoo, *Chem. Eng. J.* **2021**, *405*, 126728.
- [41] X. Guo, T. Wu, S. Zhao, Y. Fang, S. Xu, M. Xie, F. Huang, *Chem. Commun.* **2022**, *58*, 2682.
- [42] J. Luxa, P. Marvan, P. Lazar, Z. Sofer, *Nanoscale* **2019**, *11*, 14684.
- [43] J. Li, Q. Zhou, C. Yuan, P. Cheng, X. Hu, W. Huang, X. Gao, X. Wang, M. Jin, R. Nötzel, G. Zhou, Z. Zhang, J. Liu, *J. Colloid Interface Sci.* **2019**, *553*, 699.
- [44] Y. Xia, J. Huang, W. Wu, Y. Zhang, H. Wang, J. Zhu, J. Yao, L. Xu, Y. Sun, L. Zhang, R. Lu, J. Xiong, G. Zou, *ChemCatChem* **2018**, *10*, 4424.
- [45] Y. Sun, J. Meng, H. Ju, J. Zhu, Q. Li, Q. Yang, *J. Mater. Chem. A* **2018**, *6*, 22526.
- [46] I. H. Kwak, I. S. Kwon, T. T. Debela, H. G. Abbas, Y. C. Park, J. Seo, J.-P. Ahn, J. H. Lee, J. Park, H. S. Kang, *ACS Nano* **2020**, *14*, 11995.
- [47] Z. Lai, A. Chaturvedi, Y. Wang, T. H. Tran, X. Liu, C. Tan, Z. Luo, B. Chen, Y. Huang, G.-H. Nam, Z. Zhang, Y. Chen, Z. Hu, B. Li, S. Xi, Q. Zhang, Y. Zong, L. Gu, C. Kloc, Y. Du, H. Zhang, *J. Am. Chem. Soc.* **2018**, *140*, 8563.
- [48] J. Lee, S. Kang, K. Yim, K. Y. Kim, H. W. Jang, Y. Kang, S. Han, *J. Phys. Chem. Lett.* **2018**, *9*, 2049.
- [49] X. Wang, Y. Zhang, J. Wu, Z. Zhang, Q. Liao, Z. Kang, Y. Zhang, *Chem. Rev.* **2022**, *122*, 1273.
- [50] J. Hu, L. Yu, J. Deng, Y. Wang, K. Cheng, C. Ma, Q. Zhang, W. Wen, S. Yu, Y. Pan, J. Yang, H. Ma, F. Qi, Y. Wang, Y. Zheng, M. Chen, R. Huang, S. Zhang, Z. Zhao, J. Mao, X. Meng, Q. Ji, G. Hou, X. Han, X. Bao, Y. Wang, D. Deng, *Nat. Catal.* **2021**, *4*, 242.
- [51] W. Chen, J. Gu, Q. Liu, M. Yang, C. Zhan, X. Zang, T. A. Pham, G. Liu, W. Zhang, D. Zhang, B. Dunn, Y. M. Wang, *Nat. Nanotechnol.* **2022**, *17*, 153.
- [52] X. Wang, K. Yasuda, Y. Zhang, S. Liu, K. Watanabe, T. Taniguchi, J. Hone, L. Fu, P. Jarillo-Herrero, *Nat. Nanotechnol.* **2022**, *17*, 367.
- [53] S. H. Amsterdam, T. K. Stanev, L. Wang, Q. Zhou, S. Irgen-Giuro, S. Padgaonkar, A. A. Murthy, V. K. Sangwan, V. P. Dravid, E. A. Weiss, P. Darancet, M. K. Y. Chan, M. C. Hersam, N. P. Stern, T. J. Marks, *J. Am. Chem. Soc.* **2021**, *143*, 17153.
- [54] K. S. Suslick, D. A. Hammerton, R. E. Cline, *J. Am. Chem. Soc.* **1986**, *108*, 5641.
- [55] B. Jariwala, D. Voiry, A. Jindal, B. A. Chalke, R. Bapat, A. Tham-izhavel, A. Chowalla, M. Deshmukh, A. Bhattacharya, *Chem. Mater.* **2016**, *28*, 3352.
- [56] M. Hafeez, L. Gan, H. Li, Y. Ma, T. Zhai, *Adv. Mater.* **2016**, *28*, 8296.
- [57] C. Wei, R. R. Rao, J. Peng, B. Huang, I. E. L. Stephens, M. Risch, Z. J. Xu, Y. Shao-Horn, *Adv. Mater.* **2019**, *31*, 1806296.
- [58] A. A. Nurunnizar, P. Wulandari, H. Bahar, F. Fitrilawati, M. Khalil, R. Hidayat, *Mat. Sci. Semicon. Proc.* **2021**, *135*, 106095.